

Correlations and Entanglement in an Itinerant Quantum System

Andrea Bergschneider,^{*} Vincent M. Klinkhamer,[†] Jan Hendrik Becher,
Ralf Klemt, Lukas Palm, Gerhard Zürn, Selim Jochim, and Philipp M. Preiss
*Physikalisches Institut der Universität Heidelberg,
Im Neuenheimer Feld 226, 69120 Heidelberg, Germany*

Resolving the presence of entanglement and the interplay of different correlations is one of the key challenges for understanding complex quantum systems in and out of equilibrium [1, 2]. In itinerant systems, for example, the occurrence of spatial and spin entanglement is intimately connected to the competition between coherent motion and interactions [3]. With synthetic quantum systems based on ultracold atoms, the properties of such systems can be directly studied by measuring correlations in phase [4], position [5, 6], or momentum [7, 8] observables. Here, we demonstrate simultaneous spin-resolved measurements of correlation functions in two conjugate variables, namely particle position and momentum, on the single-particle level using a versatile new imaging scheme [9]. We apply this method to the fermionic Hubbard dimer, a paradigmatic example of an itinerant system containing itinerant mobile, interacting particles. From the observed mode occupations and coherences, we constrain the density matrix of the dimer [10–12] and reveal its changing nature in different interaction regimes. In particular, we directly detect entanglement in the spin and spatial modes of a Hubbard-like system [13–17]. The generic methods established in this letter can be extended to a broad range of continuum and lattice systems realized with ultracold atoms [18], and can be used to analyze correlations and entanglement in many-body phases.

To carry out our correlation measurements, we deterministically prepare quantum states with a high degree of purity. Experimentally, we realize the Hubbard dimer as two ⁶Li atoms trapped in two partially overlapping optical tweezers (Fig. 1b), with one atom per spin state $|\uparrow\rangle = |F = 1/2, m_F = -1/2\rangle$ and $|\downarrow\rangle = |F = 3/2, m_F = -3/2\rangle$, respectively. We reliably prepare this system near its ground state [19], and we can tune the tunneling rate J and the on-site interaction U via the potential depth and a Feshbach resonance, respectively.

To probe momentum correlations in this system, we release the atoms from the tweezers into a large, elongated optical dipole trap which allows expansion along the axis connecting the double well, while confining the atoms in the perpendicular directions (see Methods). We image the quantum state after a ballistic expansion for one quarter trap period which Fourier transforms the initial state to the far field. Using resonant light and separate exposures for the two spin states, we record the particle momenta k_1 and k_2 in each experimental realization (Fig. 1b). We construct the momentum correlation function $\langle n_\uparrow(k_1)n_\downarrow(k_2) \rangle$ from an average over several thousand experimental runs.

To probe the spatial correlations, we measure the occupation of each site in a spin-resolved manner. We make use of a position-mapping method, where we first project the quantum state on the single-site occupation basis by quickly decoupling the wells and then impart a site-specific momentum. This separates the spatial modes after time-of-flight for direct spatially resolved imaging (see Methods). We obtain the in-situ density distribution and determine spin-resolved correlation functions $\langle n_\uparrow(\alpha)n_\downarrow(\beta) \rangle$ (Fig. 1c), where α, β denote the spatial modes $\{L, R\}$.

Figure 2 shows the spin-resolved correlation functions for the Fermi-Hubbard dimer near its ground state for different interaction strengths (see Methods). We observe that, for the non-interacting case, the position and momentum correlation functions are separable into products of single-particle expectation values, $\langle n_\uparrow n_\downarrow \rangle \approx \langle n_\uparrow \rangle \langle n_\downarrow \rangle$. The interference pattern in the momentum-space density verifies the coherent superposition of each particle across both wells, analogous to the interference pattern of coherent light passing through a double slit. Achieving a high interference contrast is only possible with a high-fidelity ensemble preparation of a coherent quantum state.

For strong repulsive interactions, the side peaks in the momentum density $n(k)$ vanish [20], while the particles become localized and anti-correlated in position space. At the same time, pronounced oscillations in the relative-momentum axis ($d = k_1 - k_2$) appear, revealing that the purity of the quantum state is preserved in the form of two-particle coherence. This coherence can be quantified with the pair correlators in momentum space $\xi(d) = \frac{\int d\kappa \langle n_\uparrow(\kappa - d/2) n_\downarrow(\kappa + d/2) \rangle}{\int d\kappa \langle n_\uparrow(\kappa - d/2) \rangle \langle n_\downarrow(\kappa + d/2) \rangle}$ (relative momentum d) and $\chi(s) = \frac{\int d\kappa \langle n_\uparrow(\kappa + s/2) n_\downarrow(-\kappa + s/2) \rangle}{\int d\kappa \langle n_\uparrow(\kappa + s/2) \rangle \langle n_\downarrow(-\kappa + s/2) \rangle}$ (center-of-mass momentum $s = k_1 + k_2$), in analogy to noise correlation measurements in [7]. For uncorrelated particles, $\xi(d) = \chi(s) = 1$, and any deviation from this value indicates pair correlations. In our experiment, the correlators display oscillations with a contrast of up to 1.40(5) for the strongest repulsive interactions ($U/J = 18.5$, see Fig. 2c). We attribute the deviation from the maximum possible value of 2 for the ground state of the strongly repulsive Hubbard model mainly to imperfections in the expansion dynamics of our measurement procedure, rather than the actual coherence of the quantum state.

In the case of attractive interactions, qualitatively different correlations emerge: In position space, the particles almost always occupy the same site of the double well,

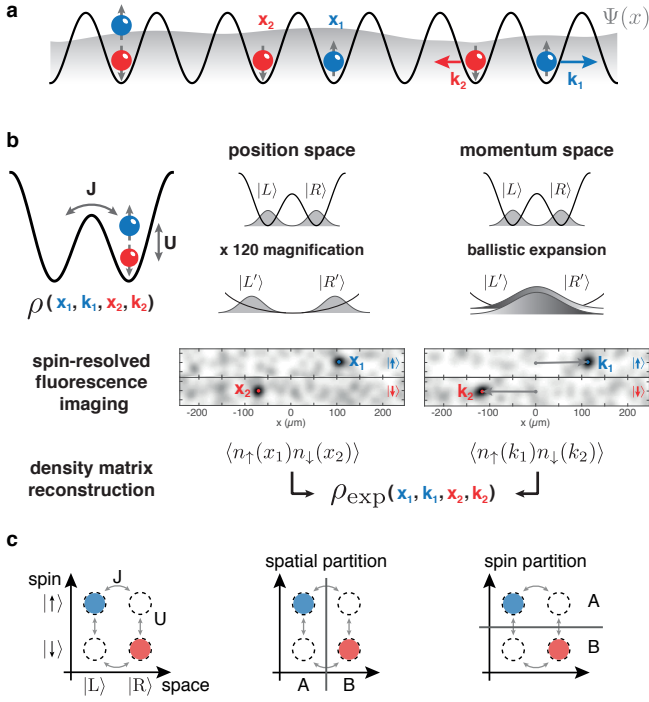


FIG 1. Detection of many-body systems in conjugate bases. a. A quantum system is defined by its many-body wavefunction $\Psi(x)$ (gray). An itinerant system can be characterized naturally with correlation functions in the positions x_i or the momenta k_i of its constituent particles. b. We measure single-particle spin-resolved correlations in position and momentum space for a two-site Fermi-Hubbard system, which we use to infer information about the density matrix ρ of the initial state. c. The spinful Hubbard dimer forms a four-mode system. Different types of quantum correlations, or entanglement, can emerge between subsystems defined by spatial or spin partitions (A and B).

while in momentum space, the coherence appears in the correlator $\chi(s)$ along the center-of-mass coordinate.

For non-vanishing interactions, the particles identified by their spin display simultaneous correlations in their position and momenta. This is a hallmark of entanglement between spin subsystems indicated in Fig. 1c. In principle, it is possible to detect entanglement directly from the magnitude of correlations between two observers, for example with a Bell test [11]. However, this test does not provide a tight witness criterion, as it may not be able to identify entangled states displaying weaker correlations. Hence, a wide range of entanglement witnesses and measures has been defined for different systems and partitions [1, 21]. For example, the previously introduced pair correlators, which encompass the one- and two-body coherences of our system, can be used to construct an entanglement witness (see Fig. 2c and Methods).

Beyond certifying its mere presence, the amount of entanglement in a quantum state is determined by entanglement measures such as the concurrence [22]. While its

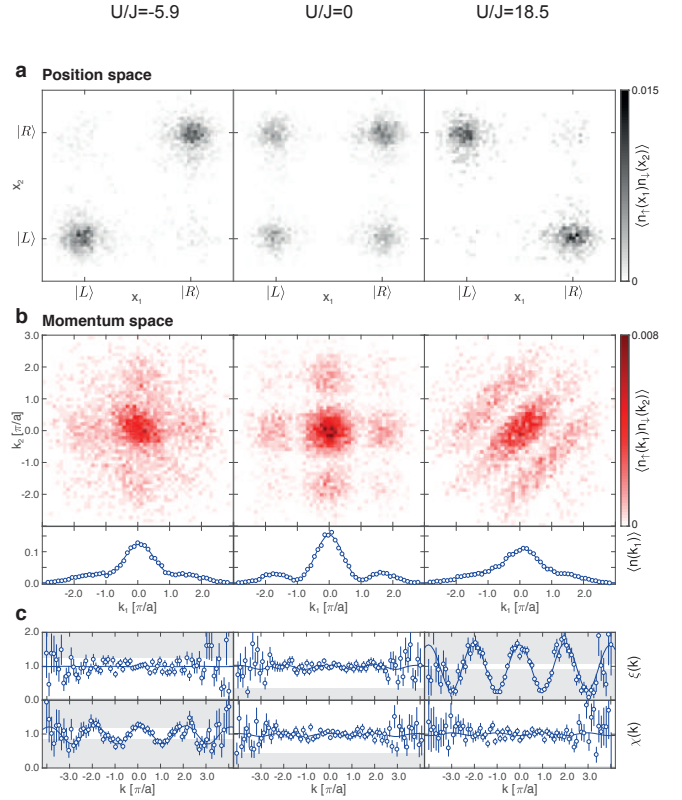


FIG 2. Correlations in the Hubbard dimer. a. The spin-resolved spatial correlation function $\langle n_{\uparrow}(\alpha)n_{\downarrow}(\beta) \rangle$ exhibits mostly double occupancies for attractive interactions (left), no correlations in the non-interacting case (center), and strong suppression of double occupancies for repulsive interactions (right). b. For non-interacting particles, the momentum-space correlation function $\langle n_{\uparrow}(k_1)n_{\downarrow}(k_2) \rangle$ (top row) is separable and shows an interference pattern in the single-particle coordinates. The single-particle coherence is visible as side peaks in the single-particle momentum density $\langle n(k_1) \rangle \equiv \langle n_{\uparrow}(k_1) \rangle + \langle n_{\downarrow}(k_1) \rangle$ (bottom row). For strong attractive (repulsive) interactions, single-particle coherence is suppressed, but interference patterns emerge along the diagonal (antidiagonal), which signals the presence of two-particle coherence. c. Integrated momentum-difference and -sum correlations, expressed as pair correlators $\chi(k)$ and $\xi(k)$, respectively. Entanglement can be certified if the data extend into the gray-shaded regions. Error bars represent the standard error of the mean and continuous lines are obtained from reconstructed momentum space correlation functions (see Methods).

exact determination requires knowledge of the full density matrix, it is possible to construct lower bounds on the concurrence from the subset of density matrix entries directly obtained from our measurements [11]. We extract these values from the interference patterns in the momentum-space correlations and from the position-space densities, respectively (Fig. 3). Writing the density matrix in a position representation $|\alpha\beta\rangle$, where α and β denote the spatial modes $\{L, R\}$ of the up and down particle, the populations

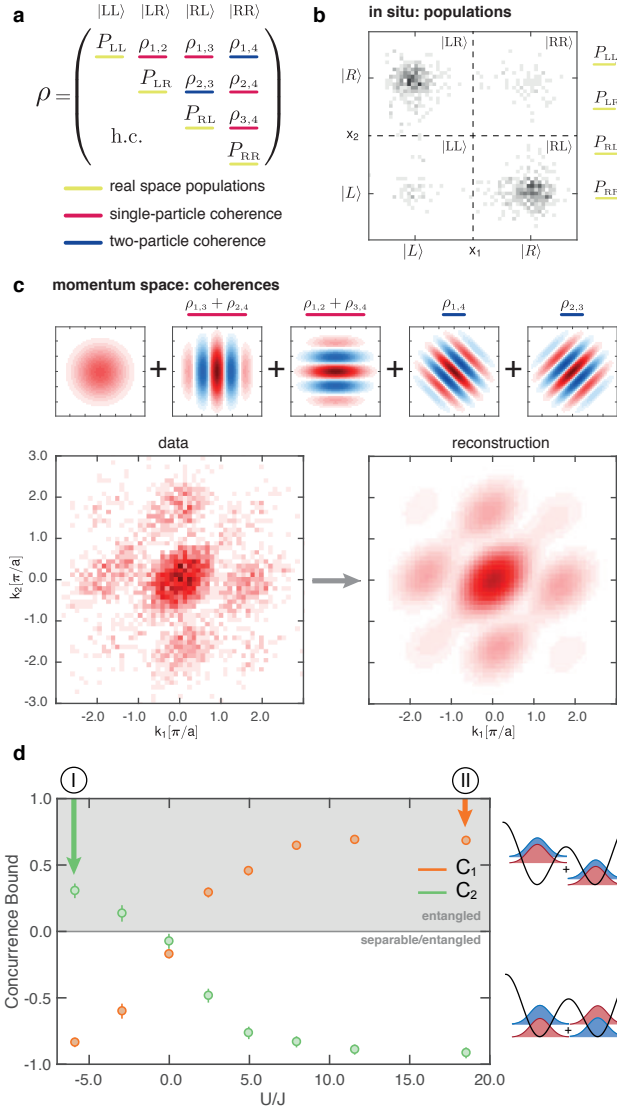


FIG 3. Evaluation of the concurrence from the measured correlation functions. **a**. The dimer density matrix ρ contains the full state information of real-space order as well as coherence properties. **b**. We obtain the *in-situ* populations directly from the position-space correlation function. **c**. The magnitude and phase of the single- and two-particle coherences are encoded in the momentum-space correlation function as oscillations along the one- and two-particle coordinates. **d**. The lower bounds C_1, C_2 of the concurrence certify entanglement (gray region) for all interacting systems studied in our experiments, with error bars corresponding to one standard deviation of statistical and systematic uncertainty (see Methods). The side panels visualize the different character of the entanglement for attractive and repulsive interactions, where the ground state approaches two-body Bell states.

and two-body coherences can be identified as the diagonal elements $\rho_{jj} \equiv P_{\alpha\beta}$ and off-diagonal elements ρ_{14}, ρ_{23} , respectively. The bounds can then be constructed as $C_1 = 2(|\rho_{23}| - \sqrt{P_{LL}P_{RR}})$ and $C_2 = 2(|\rho_{14}| - \sqrt{P_{LR}P_{RL}})$ [16, 23]. A positive value of either C_1 or C_2 results in

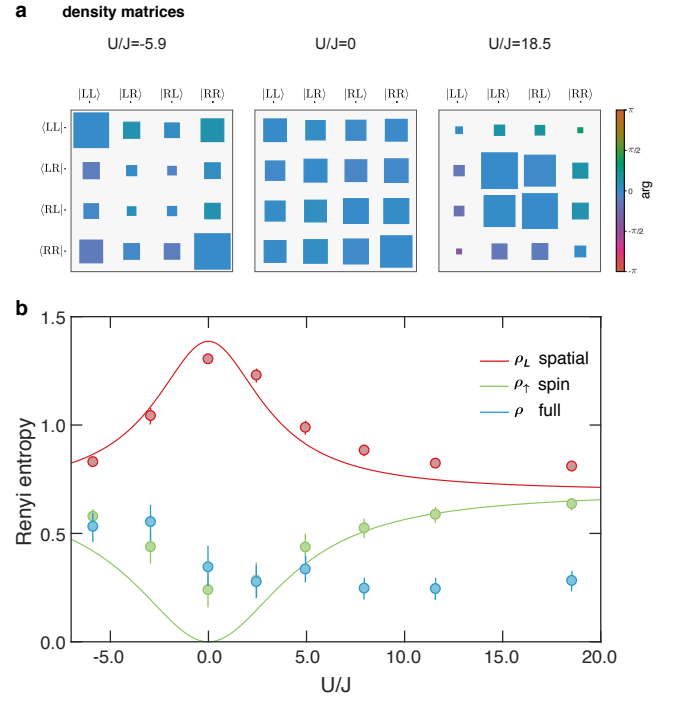


FIG 4. Entanglement entropy of the Hubbard dimer. **a**. To calculate entanglement entropy, we reconstruct the density matrix with a Bayesian quantum state estimation. The magnitude of the density matrix elements is proportional to the area of the squares, normalized to 0.5. The phase is encoded in the color scale. **b**. Entanglement can occur between different subsystems, which may be taken to be the spatial or spin modes of the Hubbard dimer defined in Fig. 1c. Entanglement is present if the Rényi entropy of a subsystem exceeds the Rényi entropy of the full system. We observe entanglement of spatial modes for all interaction strengths and entanglement of spin modes at large interaction strengths. Error bars correspond to 90 % credible intervals. The lines show the mode entropies of the ground state of the Hubbard dimer (see Methods).

a concurrence $C(\rho) \geq \max(0, C_1, C_2) > 0$, which demonstrates the presence of entanglement.

While the concurrence measures entanglement in general, the two bounds C_1 and C_2 are sensitive to different types of entangled two-particle states that occur in the Hubbard model for strong interactions (see Fig. 3d). For increasingly repulsive interactions ($U/J > 0$), the particles localize to individual wells and the spin remains as the only degree of freedom, where singlet correlations are shared across the sites. We detect this antiferromagnetic type of entanglement as $C_1 > 0$, with a maximum value of $C_1 = 0.69(2)$. For attractive interactions ($U/J < 0$), density correlations form instead, as bound pairs of $|\uparrow\rangle$ and $|\downarrow\rangle$ particles are delocalized over the system (“charge density wave”). In this case, entanglement is certified by $C_2 > 0$ with a maximum value of $C_2 = 0.31(3)$.

From these observations it is apparent that different entanglement criteria or different partitions may be sensi-

tive to different states. Using the entropy of entanglement [21], entanglement between different partitions of a larger system can be characterized systematically. For this, one measures the sub-systems separately and determines their Rényi or Von Neumann entropy. If the sub-systems individually have a higher entropy than the combined system, this proves the presence of entanglement between them [24]. Due to the generality and flexibility of this condition, the entanglement entropy is particularly useful when studying large systems containing many particles [1].

Typically, the evaluation of the entanglement entropy requires the knowledge of the full density matrix or collective measurements on multiple copies [25, 26]. For our experiment, we determine a Bayesian estimate of the density matrix given the measured position and momentum correlations (see Fig. 4a and Methods). Even with partial knowledge of the system, the physicality requirements on the density matrix lead to a tightly constrained posterior distribution of the Rényi entropy for different partitions. As shown in Fig. 4b, the Rényi entropy of individual spin modes exceeds the entropy of the full system for strong repulsive interactions, signaling the emergence of entanglement between spins with increasing interactions [17]. The entanglement between the spatial modes shows an entirely different behavior: The Rényi entropy of an individual *site* is maximal for the non-interacting system and decreases with increasing interactions. This reflects the fact that the Hilbert space of each site, which is spanned by the states $\{|0\rangle, |\uparrow\rangle, |\downarrow\rangle, |\uparrow\downarrow\rangle\}$ is most evenly populated in the case of no interactions and particle number conservation enforces correlations between sites. For repulsive interactions, as the particles become localized, the effective Hilbert space of a single site is reduced to $\{|\uparrow\rangle, |\downarrow\rangle\}$ and entropy of entanglement of the site decreases.

The disparate behavior of the entanglement entropy of sites vs. spin modes is an example of the inequivalence of entanglement between different degrees of freedom within the same state, and both concepts have a physical meaning [3, 13, 14]. The entanglement between spin modes is the relevant quantity if the quantum state were to be used for quantum information processing or communication, where each party has control over exactly one spin sector. On the other hand, the entanglement entropy of spatial regions reflects the computational cost of representing a quantum state with particle number fluctuations in real space, which may for example limit the size of DMRG simulations. Our experiment realizes and probes the smallest non-trivial quantum systems where these inequivalent notions of entanglement in itinerant systems can be explored experimentally.

The measurements show the potential of combined spin-resolved position and momentum correlation functions as a powerful tool to characterize quantum states, which can be applied both to lattice and continuum systems. By increasing the system size to a few tens of particles, new insights on many-body phenomena may be gained

[27]. With measurements in an intermediate basis (i.e., between the near-field position basis and the far-field momentum basis), it may be possible to additionally determine correlations between position and momentum modes and thereby obtain the complete density matrix [10, 28]. Among the aspects to be studied with these methods are the nature of pairing near the BEC-BCS crossover or the role and presence of high-order multipartite entanglement.

Acknowledgements We gratefully acknowledge insightful discussions with Andrew Daley, Andreas Elben, Martin Gärttner, Philipp Hauke, and Marco Piani. This work has been supported by the ERC consolidator grant 725636, the Heidelberg Center for Quantum Dynamics and is part of the DFG Collaborative Research Centre SFB 1225 (ISOQUANT). A. B. acknowledges funding from the International Max-Planck Research School (IMPRS-QD). P.M.P. acknowledges funding from European Unions Horizon 2020 programme under the Marie Skłodowska-Curie grant agreement No. 706487.

A. B. and V. M. K. contributed equally to this work.

* bergschneider@physi.uni-heidelberg.de;

Present address: Institut für Quantenelektronik, Auguste-Piccard-Hof 1, 8093 Zürich, Switzerland

† klinkhamer@physi.uni-heidelberg.de

- [1] L. Amico, A. Osterloh, and V. Vedral, *Rev. Mod. Phys.* **80**, 517 (2008).
- [2] A. Lukin, M. Rispoli, R. Schittko, M. E. Tai, A. M. Kaufman, S. Choi, V. Khemani, J. Léonard, and M. Greiner, “Probing entanglement in a many-body-localized system,” arXiv:1805.09819 (2018).
- [3] M. C. Tichy, F. Mintert, and A. Buchleitner, *J. Phys. B At. Mol. Opt. Phys.* **44**, 192001 (2011).
- [4] T. Schweigler, V. Kasper, S. Erne, I. Mazets, B. Rauer, F. Cataldini, T. Langen, T. Gasenzer, J. Berges, and J. Schmiedmayer, *Nature* **545**, 323 (2017).
- [5] M. Endres, M. Cheneau, T. Fukuhara, C. Weitenberg, P. Schauss, C. Gross, L. Mazza, M. C. Banuls, L. Pollet, I. Bloch, and S. Kuhr, *Science* **334**, 200 (2011).
- [6] C. Gross and I. Bloch, *Science* **357**, 995 (2017).
- [7] S. Fölling, F. Gerbier, A. Widera, O. Mandel, T. Gericke, and I. Bloch, *Nature* **434**, 481 (2005).
- [8] S. S. Hodgman, R. I. Khakimov, R. J. Lewis-Swan, A. G. Truscott, and K. V. Kheruntsyan, *Phys. Rev. Lett.* **118**, 240402 (2017).
- [9] A. Bergschneider, V. M. Klinkhamer, J. H. Becher, R. Klemt, G. Zürn, P. M. Preiss, and S. Jochim, *Phys. Rev. A* **97**, 063613 (2018).
- [10] G. Taguchi, T. Dougakiuchi, N. Yoshimoto, K. Kasai, M. Iinuma, H. F. Hofmann, and Y. Kadoya, *Phys. Rev. A* **78**, 012307 (2008).
- [11] M. Bonneau, W. J. Munro, K. Nemoto, and J. Schmiedmayer, “Characterizing two-particle entanglement in a double-well potential,” arXiv:1711.08977 (2017).
- [12] V. M. Klinkhamer, *Few-Fermion Systems under a Matterwave Microscope*, Phd thesis, Heidelberg University

- (2018).
- [13] P. Zanardi, Phys. Rev. A **65**, 042101 (2002).
 - [14] M. R. Dowling, A. C. Doherty, and H. M. Wiseman, Phys. Rev. A **73**, 052323 (2006).
 - [15] L. Neves, G. Lima, E. J. S. Fonseca, L. Davidovich, and S. Pádua, Phys. Rev. A **76**, 032314 (2007).
 - [16] A. M. Kaufman, B. J. Lester, M. Foss-Feig, M. L. Wall, A. M. Rey, and C. A. Regal, Nature **527**, 208 (2015).
 - [17] N. M. Linke, S. Johri, C. Figgatt, K. A. Landsman, A. Y. Matsuura, and C. Monroe, “Measuring the Renyi entropy of a two-site Fermi-Hubbard model on a trapped ion quantum computer,” arXiv:1712.08581 (2017).
 - [18] I. Bloch, J. Dalibard, and W. Zwerger, Rev. Mod. Phys. **80**, 885 (2008).
 - [19] S. Murmann, A. Bergschneider, V. M. Klinkhamer, G. Zürn, T. Lompe, and S. Jochim, Phys. Rev. Lett. **114**, 080402 (2015).
 - [20] M. Greiner, O. Mandel, T. Esslinger, T. W. Hänsch, and I. Bloch, Nature **415**, 39 (2002).
 - [21] R. Horodecki, P. Horodecki, M. Horodecki, and K. Horodecki, Rev. Mod. Phys. **81**, 865 (2009).
 - [22] W. K. Wootters, Phys. Rev. Lett. **80**, 2245 (1998).
 - [23] M. Jafarpour and A. Sabour, Quantum Inf. Process. **11**, 1389 (2012).
 - [24] F. Mintert and A. Buchleitner, Phys. Rev. Lett. **98**, 140505 (2007).
 - [25] H. Pichler, L. Bonnes, A. J. Daley, A. M. Läuchli, and P. Zoller, New J. Phys. **15**, 063003 (2013).
 - [26] R. Islam, R. Ma, P. M. Preiss, M. Eric Tai, A. Lukin, M. Rispoli, and M. Greiner, Nature **528**, 77 (2015).
 - [27] J. Bjerlin, S. M. Reimann, and G. M. Bruun, Phys. Rev. Lett. **116**, 155302 (2016).
 - [28] G. Taguchi, T. Dougakiuchi, M. Iinuma, H. F. Hofmann, and Y. Kadoya, Phys. Rev. A **80**, 062102 (2009).
 - [29] F. Serwane, G. Zürn, T. Lompe, T. B. Ottenstein, A. N. Wenz, and S. Jochim, Science **332**, 336 (2011).
 - [30] W. K. Wootters, Quantum Inf. Comput. **1**, 27 (2001).
 - [31] R. Blume-Kohout, New J. Phys. **12**, 043034 (2010).

SUPPLEMENTAL MATERIAL

Experimental sequence and parameters For our experiments we use two of the three lowest Zeeman sublevels of the hyperfine ground state of ^6Li , labeled $|1\rangle$ and $|3\rangle$ in order of increasing energy. We realize a double-well potential with two optical tweezers of far-red-detuned laser light at 1064 nm. We generate and control the tweezers with an acousto-optical-deflector (AOD). This allows us to individually control each well of the double-well system. In order to prepare the system in its ground state, we deterministically prepare two atoms of different spin (labeled $|\uparrow\rangle \equiv |1\rangle$ and $|\downarrow\rangle \equiv |3\rangle$) in the ground state of a single tweezer [29]. Following the procedure described in [19], we ramp on the second well and perform an adiabatic Landau-Zener passage to the ground state of the symmetric double-well. This system forms a Hubbard dimer, where we can tune the tunnel coupling J by changing the global depth of the optical potential and the on-site interaction U with a Feshbach resonance.

All presented measurements are performed in a double-well with a separation of $a = 1.5\ \mu\text{m}$ along the x -axis. Each tweezer has a waist of $1.15\ \mu\text{m}$ and single well trap frequencies of $\omega_z = 2\pi \times 3.95(10)\ \text{kHz}$ along the axial and $\omega_{x,y} = 2\pi \times 18.8(4)\ \text{kHz}$ along the in-plane directions, respectively. With this configuration, we achieve tunneling rates of $J/h = 77(1)\ \text{Hz}$, where h is Planck's constant.

In order to extract the in-situ populations and the momenta of the atoms, we employ a single-atom, spin-resolved imaging technique [9].

Momentum measurements We measure the momentum of the atoms using a time-of-flight technique. After preparing the system, the quantum state is allowed to expand in a weak optical potential (optical dipole trap, ODT) which is elongated along the double-well axis with a longitudinal trap frequency of $\omega_x = 2\pi \times 75\ \text{Hz}$ and transverse trap frequencies of $\omega_{y,z} = 2\pi \times 600\ \text{Hz}$ (Extended Data Fig. 5a). We image the atoms after a quarter of the axial trap period, $T_{\text{ODT}}/4 = \frac{\pi}{2\omega_x}$. As the interactions during time of flight are negligible, the unitary evolution in the dipole trap exactly performs a Fourier transform of the single-particle wavefunction in the x -direction. Neglecting the y and z coordinates, which are integrated out in the data analysis and imaging process, respectively, we obtain the initial momentum distribution along the double-well axis by a simple rescaling of the particle coordinates after time-of-flight, $k_{1,2}/k_{\text{lat}} = qx_{1,2}$, where $k_{\text{lat}} = \pi/a$ is the lattice momentum. We determine the scale factor from a fit as $q = 20.1\ \text{mm}^{-1}$, which is consistent with the trap frequency ω_x during time-of-flight. The spin-resolved correlation function $\langle n_{\uparrow}(k_1)n_{\downarrow}(k_2) \rangle$ is obtained by averaging spin-resolved momentum measurements over several thousand runs. Note that the symmetry of the correlation functions (Fig. 2 and Extended Data Fig. 9) directly stems from the symmetries of the quantum state.

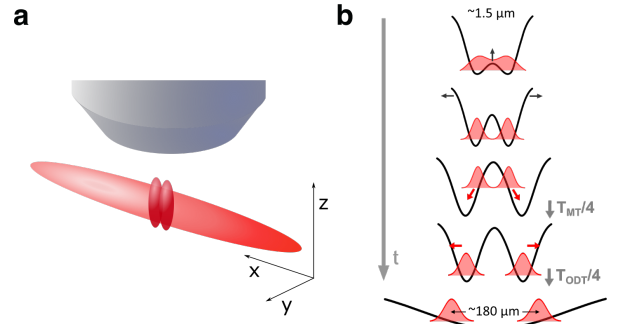


FIG 5. Scheme for position-space measurements. **a** With the high-resolution objective, we create a double-well potential consisting of two adjacent optical tweezers. The double well is aligned along the long axis of the waveguide potential created by our optical dipole trap. **b** In order to extract the in-situ populations, we suddenly increase the trap depth and separate the wells. After a $T_{\text{MT}}/4$ time evolution in the double-well potential, the atoms are released from the tweezers. An additional $T_{\text{ODT}}/4$ evolution in the optical waveguide potential increases the separation between the spatial modes by a factor of 120. Note that the spatial dimensions in this figure are not to scale.

Position measurements The resolution of our imaging technique is limited to $4\ \mu\text{m}$ [9]. Therefore, we cannot directly measure the in-situ distribution of the double-well system. In order to reconstruct the position space distribution, we thus perform a three step scheme as illustrated in Extended Data Fig. 5b). First, we project the wavefunction onto the individual wells by diabatically increasing the trap depth of the double-well to $\omega_{x,y} \approx 2\pi \times 41.6\ \text{kHz}$ within 2 ms, decoupling the wells completely. Then we imprint a distinct and diametrical center of mass momentum onto the on-site wavefunctions of the two wells. We achieve this by a sudden change in the well separation to $3.2\ \mu\text{m}$ with a subsequent time evolution of around $6\ \mu\text{s}$ corresponding to a quarter of the on-site trap period T_{MT} . In the final step, we switch off the double-well potential followed by a time-of-flight evolution in the ODT (longitudinal trap frequency $\omega_x \approx 2\pi \times 225\ \text{Hz}$). By tuning the trap depth of the individual wells, their final separation, and the trap frequency of the ODT, we can optimize the magnification of the on-site wavefunction and the magnification of the well separation independently. For the parameters used in this paper, we separate the center of mass of the on-site wavefunction by approximately $180\ \mu\text{m}$ and achieve a fidelity for identifying each atom in the correct well of $99.4(3)\ \%$.

Data analysis and data set Each data set corresponds to ~ 4000 momentum and ~ 1000 position measurements. We postselect our data for images with exactly one atom per spin state, corresponding to $\geq 80\ \%$ of all images. Before analysis, we group atom positions into 2 pixel (or $5.4\ \mu\text{m}$) bins.

In total we measured the position and momentum cor-

relation functions for 8 different values of U/J , ranging from attractive interaction ($U/J = -5.9$ at 525 G) to strong repulsive interaction ($U/J = 18.5$ at 625 G). Our full dataset is shown in Extended Data Fig. 9. All measurements are performed at a fixed tunnel coupling of $J/h = 77(1)$ Hz. The on-site interaction strength U is set by the trap geometry and the s-wave scattering length a_{sc} which we set below a Feshbach resonance at $B = 690$ G. Both tunnel coupling and on-site interaction strength are calibrated as described in [19].

Hubbard dimer Our system can be described by the Hubbard Hamiltonian

$$H = -J \sum_{\sigma} \left(\hat{c}_{L\sigma}^{\dagger} \hat{c}_{R\sigma} + \hat{c}_{R\sigma}^{\dagger} \hat{c}_{L\sigma} \right) + U \sum_{j=L,R} \hat{n}_{j\downarrow} \hat{n}_{j\uparrow}, \quad (1)$$

where $\hat{c}_{i\sigma}^{(\dagger)}$ is the fermionic annihilation (creation) operator of a particle with pseudospin σ on site i and $\hat{n}_{j\sigma} = \hat{c}_{j\sigma}^{\dagger} \hat{c}_{j\sigma}$. Its ground state can be written as

$$\psi_1 = (1, \alpha_+(x), \alpha_+(x), 1) / \sqrt{2(1 + \alpha_+(x)^2)} \quad (2)$$

in a position space basis given by

$$\begin{aligned} |LL\rangle &= c_{\uparrow L}^{\dagger} c_{\downarrow L}^{\dagger} |0\rangle \\ |LR\rangle &= c_{\uparrow L}^{\dagger} c_{\downarrow R}^{\dagger} |0\rangle \\ |RL\rangle &= c_{\uparrow R}^{\dagger} c_{\downarrow L}^{\dagger} |0\rangle \\ |RR\rangle &= c_{\uparrow R}^{\dagger} c_{\downarrow R}^{\dagger} |0\rangle, \end{aligned} \quad (3)$$

with $x = U/4J$ and $\alpha_{\pm}(x) = x \pm \sqrt{1 + x^2}$ [13].

A general (mixed) state takes the form

$$\rho = \begin{pmatrix} P_{LL} & \rho_{1,2} & \rho_{1,3} & \rho_{1,4} \\ & P_{LR} & \rho_{2,3} & \rho_{2,4} \\ & & P_{RL} & \rho_{3,4} \\ \text{h.c.} & & & P_{RR} \end{pmatrix}, \quad (4)$$

where $P_{\alpha,\beta}$ are the populations and $\rho_{i,j}$ are the coherences.

Evaluation of density matrix elements If we wish to determine the measured density matrix ρ_{exp} of a prepared state ρ , we can directly read off the populations from the spatial correlation measurements, while we can extract the coherences from the momentum correlation measurements as outlined in [11, 12] (Fig. 3a-c). To calculate the momentum correlation functions for ρ , we use the Fourier transform of the single-particle basis states,

$$\begin{aligned} \phi_L &\equiv g(x + a/2) \xrightarrow{FT} \tilde{g}(k) e^{-iak/2} \\ \phi_R &\equiv g(x - a/2) \xrightarrow{FT} \tilde{g}(k) e^{iak/2}. \end{aligned} \quad (5)$$

Here, $g(x)$ is the on-site Wannier function, which is very well approximated by a Gaussian within the precision of the experiment. The momentum space representations of the single-particle modes share the envelope $\tilde{g}(k)$ (given by the Fourier transform of the on-site wavefunction $g(x)$) and differ only by a differential phase gradient e^{iak} . In

the basis defined by Eq. (3) the momentum correlation operator $\hat{Z} = \hat{n}_{\uparrow}(k_1) \hat{n}_{\downarrow}(k_2)$ takes on the matrix representation

$$\hat{Z} = \begin{pmatrix} 1 & e^{-iak_2} & e^{-iak_1} & e^{-ia(k_1+k_2)} \\ & 1 & e^{-ia(k_1-k_2)} & e^{-iak_1} \\ & & 1 & e^{-iak_2} \\ \text{h.c.} & & & 1 \end{pmatrix}, \quad (6)$$

where we have neglected the envelope $\tilde{g}(k)$.

Using the momentum basis (5), the expectation value of the operator \hat{Z} can be calculated as

$$\begin{aligned} \langle n_{\uparrow}(k_1) n_{\downarrow}(k_2) \rangle &= \text{Tr}(\rho \hat{Z}) \\ &= P_{LL} + P_{LR} + P_{RL} + P_{RR} \\ &\quad + 2 \Re \left\{ \rho^{(1)} e^{iak_1} \right\} \\ &\quad + 2 \Re \left\{ \rho^{(2)} e^{iak_2} \right\} \\ &\quad + 2 \Re \left\{ \rho_{2,3} e^{ia(k_1-k_2)} \right\} \\ &\quad + 2 \Re \left\{ \rho_{1,4} e^{ia(k_1+k_2)} \right\}, \end{aligned} \quad (7)$$

with $\rho^{(1)} = \rho_{1,3} + \rho_{2,4}$, $\rho^{(2)} = \rho_{1,2} + \rho_{3,4}$ and $P_{LL} + P_{LR} + P_{RL} + P_{RR} = \text{Tr}(\rho) = 1$.

For our data analysis, we use the quadrature representation

$$\begin{aligned} \langle n_{\uparrow}(k_1) n_{\downarrow}(k_2) \rangle &= 1 \\ &\quad + 2 \Re \{ (\rho_{1,3} + \rho_{2,4}) \} \cos ak_1 \\ &\quad - 2 \Im \{ (\rho_{1,3} + \rho_{2,4}) \} \sin ak_1 \\ &\quad + 2 \Re \{ (\rho_{1,2} + \rho_{3,4}) \} \cos ak_2 \\ &\quad - 2 \Im \{ (\rho_{1,2} + \rho_{3,4}) \} \sin ak_2 \\ &\quad + 2 \Re \{ \rho_{2,3} \} \cos a(k_1 - k_2) \\ &\quad - 2 \Im \{ \rho_{2,3} \} \sin a(k_1 - k_2) \\ &\quad + 2 \Re \{ \rho_{1,4} \} \cos a(k_1 + k_2) \\ &\quad - 2 \Im \{ \rho_{1,4} \} \sin a(k_1 + k_2), \end{aligned} \quad (8)$$

where the real and imaginary parts of the density matrix elements now explicitly appear as coefficients of the trigonometric basis functions of the momentum-space correlation function $\langle n_{\uparrow}(k_1) n_{\downarrow}(k_2) \rangle$.

To obtain the off-diagonal matrix elements $\rho_{1,4}, \rho_{2,3}, \dots$, we generate a reconstruction \mathbf{R} of the measured momentum correlation functions \mathbf{D} in terms of the known basis functions \mathbf{B} , shown in Extended Data Fig. 6. We are looking for the weights w such that the reconstruction $\mathbf{R} = \sum_i w_i \mathbf{B}_i$ minimizes the total square error to the data, $\epsilon = [(\mathbf{R} - \mathbf{D}) | (\mathbf{R} - \mathbf{D})]$. Here quantities in bold are defined in the two-particle coordinate space spanned by k_1 and k_2 and $[\cdot | \cdot]$ denotes bin-wise multiplication and summation over the entire space. Even though the basis functions \mathbf{B}_i are not perfectly orthogonal to each other due to the finite envelope function, a closed form for the optimal weights can be given as $w_{\text{opt}} = Q^{-1} L$, where the matrix Q quantifies the overlap of the basis functions via

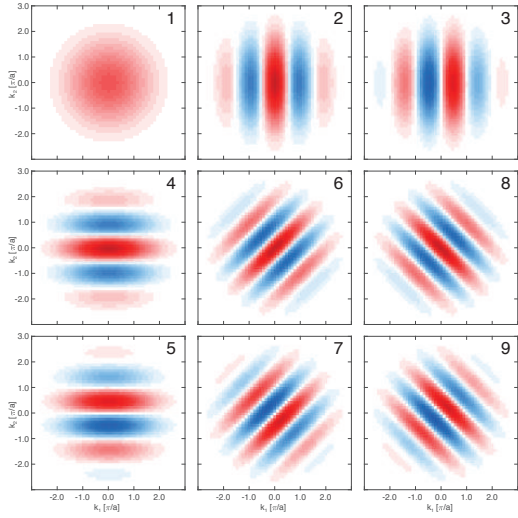


FIG 6. Basis functions \mathbf{B}_i used for the reconstruction of momentum correlations. We obtain the envelope and fringe spacing from fits to single-particle density profiles after time-of-flight. The indices correspond to the lines in Eq. 8.

$Q_{ij} = [\mathbf{B}_i | \mathbf{B}_j]$ and L is the overlap vector between the basis functions and the data, $L_i = [\mathbf{B}_i | \mathbf{D}]$. The optimal reconstruction for all data sets is shown in Extended Data Fig. 9. From the weights w we read off the complex-valued off-diagonal density matrix elements according to Eq. (8). The matrix elements $\rho_{1,3}$ and $\rho_{2,4}$ (as well as $\rho_{1,2}$ and $\rho_{3,4}$) contribute to the same features in the two-particle correlation functions and our measurements only reveal their complex sum. Combining measurements from position and momentum space, we obtain 12 of the 16 real coefficients defining the density matrix.

The dominant source of systematic errors on the optimal weights w_{opt} are uncertainties in the fringe spacing as well as envelope waist and center in the basis functions \mathbf{B} . These parameters as well as their uncertainties are obtained from a fit to the single-particle density distributions $\langle n(k) \rangle$ for the non-interacting data. We perform the reconstruction of $\langle n_{\uparrow}(k_1)n_{\downarrow}(k_2) \rangle$ 8000 times with basis function parameters randomly sampled from a normal distribution representing their uncertainty. The systematic error on the density matrix entries is given by their standard deviation over all instances of the basis function parameters.

We separately estimate the statistical error on the optimal weights w_{opt} by resampling the measured two-particle probability distribution $\langle n_{\uparrow}(k_1)n_{\downarrow}(k_2) \rangle$ 1000 times with fixed basis function parameters, assuming independent shot noise in each bin. For each instance of the distribution, we obtain the reconstruction and the corresponding weights. The statistical error on the density matrix entries is given by the standard deviation of the distribution over all resampled instances. The reported errors on individual density matrix entries are quadrature sums of the

systematic and statistical error bars.

We calculate the theory lines for the momentum density $\langle n(k_1) \rangle \equiv \langle n_{\uparrow}(k_1) \rangle + \langle n_{\downarrow}(k_1) \rangle$ and correlators $\chi(s)$ and $\xi(d)$ by performing the corresponding integrals over the reconstruction \mathbf{R} .

Entanglement witness from correlators A very direct way to witness entanglement between spin modes is provided by analysing the correlators $\chi(s)$ and $\xi(d)$ and comparing their amplitudes to limits compatible with separable states. From Eq. (7), the single-particle densities are given by $n_{\uparrow}(k_1) = 1 + 2 \Re\{\rho^{(1)}e^{iak_1}\}$ and $n_{\downarrow}(k_2) = 1 + 2 \Re\{\rho^{(2)}e^{iak_2}\}$. The correlators take the form

$$\xi(d) = \frac{1 + 2|\rho_{2,3}|\cos(ad + \phi_{2,3})}{1 + 2|\rho^{(1)}||\rho^{(2)}|\cos(ad - \phi^{(1)} + \phi^{(2)})}, \quad (9)$$

where we have written the complex density matrix elements in polar representation, $\rho_j = |\rho_j|e^{i\phi_j}$.

We follow [16] to find the maximum contrast in ξ . For a single product state, i.e., $\rho^{(\text{prod})} = \rho^{(\uparrow)} \otimes \rho^{(\downarrow)}$, triangle inequalities on the density matrix imply that

$$\begin{aligned} |\rho_{2,3}^{(\text{prod})}| &\leq |\rho_{1,2}^{(\uparrow)}| |\rho_{2,1}^{(\downarrow)}| \\ &\leq \sqrt{\rho_{1,1}^{(\uparrow)}\rho_{2,2}^{(\uparrow)}} \sqrt{\rho_{1,1}^{(\downarrow)}\rho_{2,2}^{(\downarrow)}} \\ &= \sqrt{P_{\text{RR}}P_{\text{LL}}} = \sqrt{P_{\text{LR}}P_{\text{RL}}}, \end{aligned} \quad (10)$$

where we choose the tighter bound $\sqrt{P_{\text{RR}}P_{\text{LL}}}$.

For the most general form of a mixed state, $\rho^{(\text{mix})} = \sum_i \lambda_i \rho^{(i,\uparrow)} \otimes \rho^{(i,\downarrow)}$, one still finds that

$$|\rho_{2,3}^{(\text{mix})}| \leq \sqrt{P_{\text{RR}}P_{\text{LL}}}. \quad (11)$$

The in-situ occupation probabilities hence set an upper bound on the modulus of $\rho_{2,3}$ [16].

The strongest correlations that are compatible with a separable state are then given by

$$\begin{aligned} \xi_{\text{max}} &= \frac{1 + 2\sqrt{P_{\text{RR}}P_{\text{LL}}}}{1 - 2|\rho^{(1)}||\rho^{(2)}|} \\ \xi_{\text{min}} &= \frac{1 - 2\sqrt{P_{\text{RR}}P_{\text{LL}}}}{1 + 2|\rho^{(1)}||\rho^{(2)}|}, \end{aligned} \quad (12)$$

with similar expressions for $\chi(s)$. The upper and lower bounds on the correlators under the assumption of separability are shown as the gray shaded area in Fig. 2c.

Concurrence We can use a lower bound of the concurrence C to quantify the amount of entanglement in our system. For a pair of two-level systems (qubits), the concurrence can be used to obtain the entanglement of formation. In the case of a pure two-qubit state Φ , C is formally defined as $C(\Phi) = |\langle \Phi | (\sigma_y \otimes \sigma_y) | \Phi^* \rangle|$ [30] with the Pauli matrix $\sigma_y = \begin{pmatrix} 0 & -i \\ i & 0 \end{pmatrix}$. For a mixed state, one

defines the concurrence as the infimum of its value over all pure state decompositions

$$C(\rho) = \inf \sum_i p_i C(\Phi_i). \quad (13)$$

In the special case of a pair of qubits one can find the explicit formula

$$C(\rho) = \max\{0, \lambda_1 - \lambda_2 - \lambda_3 - \lambda_4\} \quad (14)$$

where λ_i^2 , $i \in \{1, 2, 3, 4\}$, are the eigenvalues of $\rho(\sigma_y \otimes \sigma_y)\rho^*(\sigma_y \otimes \sigma_y)$ in decreasing order. $C(\rho)$ can take values from 0 for a product state to 1 for a maximally entangled state. A positive value of the concurrence indicates the presence of entanglement in the system. In particular, for a two-qubit system, the entanglement of formation can directly be calculated from the concurrence [30].

For our purposes, we follow [23] to construct a lower bound for the concurrence and hence for the entanglement of formation as:

$$C(\rho) \geq \max\{0, 2(|\rho_{1,4}| - \sqrt{P_{LR}P_{RL}}), 2(|\rho_{2,3}| - \sqrt{P_{LL}P_{RR}})\}. \quad (15)$$

Hence, from the matrix elements obtained from position and momentum space correlations, we can directly calculate the lower bounds of the concurrence (see Fig. 3d).

Measurement of the full density matrix Complete knowledge of the density matrix can in principle be obtained by performing rotations on the state prior to measurement. Reference [11] suggests to apply pulses of pure tunneling or tilt to the double-well. We point out that it is also possible to use a pulse with interaction only, i.e. to apply Hamiltonian (1) with $J = 0$ for a time $t = \frac{1}{4} \frac{\hbar}{U}$, which allows the measurement of the complex differences $\rho_{1,3} - \rho_{2,4}$ etc. and completes the measurement of all entries of the density matrix.

Alternatively, correlated position-momentum measurements would deliver the density matrix elements complementary to the entries obtained from pure position and momentum correlation measurements [10]. These measurements could, for example, be performed in an intermediate basis.

Reconstruction of the density matrix From the previously described methods, we obtain only a subset of the parameters required to unambiguously describe the density matrix of the prepared state. This means that there is a set of density matrices which would be consistent with the measured parameters. Also, we determine these parameters with statistical and systematic uncertainties, which can lead to unphysical properties for an entire set of density matrices consistent with ρ_{exp} . For example, their eigenvalues with small magnitudes may consistently turn out to be negative.

To avoid these unphysical sets of density matrices, we reconstruct the density matrix ρ_{BME} using a Bayesian

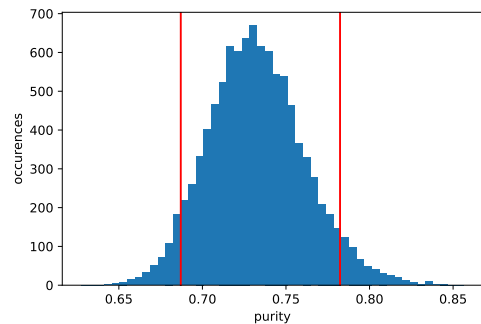


FIG 7. Posterior distribution of the full system purity V . The reconstructed density matrix is obtained from measurements performed at $U/J = 18.5$. The red lines mark the 90 % credible interval.

quantum state estimation as outlined in [31]. All information about the experiment is contained in the likelihood function $\mathcal{L}(\rho) = p(\mathcal{M}|\rho)/p(\mathcal{M})$, a distribution over the measured data \mathcal{M} conditioned on a certain hypothesis about the state ρ . It quantifies the relative plausibility of different possible states. In the case of Gaussian distributed errors, it takes the form

$$\mathcal{L}(\rho) = \prod_j \frac{1}{\sqrt{2\pi\sigma_j^2}} \exp\left(-\frac{(\mathcal{M}_j - \text{Tr}[\hat{\mathcal{M}}_j\rho])^2}{2\sigma_j^2}\right) \quad (16)$$

with the set of measurements $\mathcal{M} = \{\mathcal{M}_j\}$ and corresponding errors σ_j . It contains the four real-valued populations and the complex coherences defined as coefficients in Eq. 8. The corresponding operators $\hat{\mathcal{M}}_j$ denote the projections of the state onto these entries. To obtain the posterior distribution $\pi_f(\rho)d\rho$, the likelihood is multiplied with a prior distribution $\pi_0(\rho)d\rho$ on the states:

$$\pi_f(\rho)d\rho \propto \mathcal{L}(\rho)\pi_0(\rho)d\rho \quad (17)$$

where the proportionality is up to normalization. Because no prior knowledge on the states is assumed, we choose the Hilbert-Schmidt prior as an uninformative prior over all density matrices that meet the requirements of positive definiteness and unity trace. The Bayesian mean estimate $\hat{\rho}_{\text{BME}}$ is then given by the mean of the posterior distribution

$$\hat{\rho}_{\text{BME}} = \int \rho \pi_f(\rho) d\rho. \quad (18)$$

The expectation value of an observable \mathcal{O} can be calculated as $\langle \mathcal{O} \rangle = \int \mathcal{O}(\rho) \pi_f(\rho) d\rho$ with the errors given in terms of the credible interval of its posterior distribution. An example of this can be seen in Extended Data Fig. 7 for the purity.

To compute $\hat{\rho}_{\text{BME}}$, we first parametrize the density matrix as $\rho = \hat{T}^\dagger \hat{T}$ where \hat{T} is a random complex matrix with 32 real parameters \mathbf{t} . This form ensures that

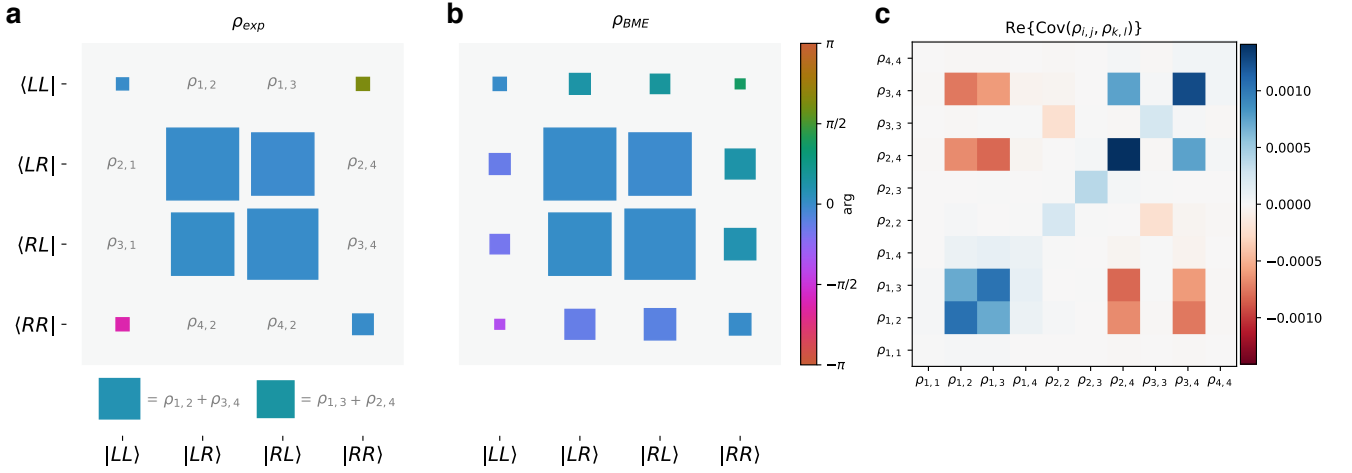


FIG 8. Density matrix reconstruction. **a** Measured density matrix at $U/J = 18.5$, obtained from the spatial measurements and from fitting the momentum correlations. The magnitude of the entries is proportional to the area of the squares and normalized to 0.5, while the phase is indicated by the color scale. **b** Reconstructed density matrix obtained from the Bayesian mean estimate. **c** Real part of the covariance of the reconstructed density matrix elements obtained from sampling. While the diagonal elements are correlated by the condition $\text{Tr } \rho = 1$, some off-diagonal elements are anti-correlated due to, e.g., $\rho^{(1)} = \rho_{1,3} + \rho_{2,4}$.

$\rho(\mathbf{t})$ is a positive semidefinite and Hermitian matrix of trace one. We sample the posterior using Hamiltonian Monte Carlo (HMC) to compute $\hat{\rho}_{\text{BME}}$ and the subsequent entanglement measures and determine their uncertainty.

In the experiment, not all entries of ρ_{exp} are measured individually. For $\rho_{1,2}, \rho_{2,4}$ and $\rho_{2,3}, \rho_{3,4}$ only the sums are determined. This can be incorporated naturally in the Bayesian estimation by specifying the set of measurements \mathcal{M} accordingly. The HMC procedure then samples the space of physically possible entries while leaving the corresponding sum unchanged. The uncertainty about the entanglement measures with respect to the exact distribution of the sum constituents is therefore expressed in the credible intervals of these values.

The covariances of $\rho_{i,j}$ shown in Extended Data Fig. 8 support this intuition, as the variance is largest for $\rho_{2,4}$ (and $\rho_{3,4}$) while being most anticorrelated with $\rho_{1,2}$ ($\rho_{2,3}$ respectively).

Rényi entropy With our Bayesian estimate of the density matrix, we can evaluate the expected value of the Rényi entropy $S = -\log \text{Tr}(\rho^2)$ for the entire system and for different sub-systems. In our definition, we use the natural logarithm, and $\text{Tr}(\rho^2) \equiv V$ can be identified as the purity.

The entanglement between the spin modes is obtained

by tracing out one of the two particles. In term of the full-system density matrix in Eq. (4), the single-spin density matrix is given by

$$\rho_{\uparrow} = \begin{pmatrix} P_{LL} + P_{LR} & \rho_{1,3} + \rho_{2,4} \\ \text{h.c.} & P_{RL} + P_{RR} \end{pmatrix} \quad (19)$$

with the single-spin Rényi entropy $S_{\uparrow} = -\log \text{Tr}(\rho_{\uparrow}^2)$. Note that the single-spin entropy depends only on the sum of the matrix elements $\rho_{1,3} + \rho_{2,4}$ as well as the populations and can be extracted directly from our measurements.

The single-site density matrix in the basis $|\uparrow\downarrow\rangle, |\uparrow\rangle, |\downarrow\rangle, |0\rangle$ is

$$\rho_L = \begin{pmatrix} P_{LL} & & & \\ & P_{LR} & & \\ & & P_{RL} & \\ & & & P_{RR} \end{pmatrix}$$

i.e. it has only the populations, but no coherences and we calculate its entropy as $S_L = -\log \text{Tr}(\rho_L^2)$.

In Fig. 4b, we compare the measured entanglement entropies to the Hubbard model using the density matrix from Eq. (2).

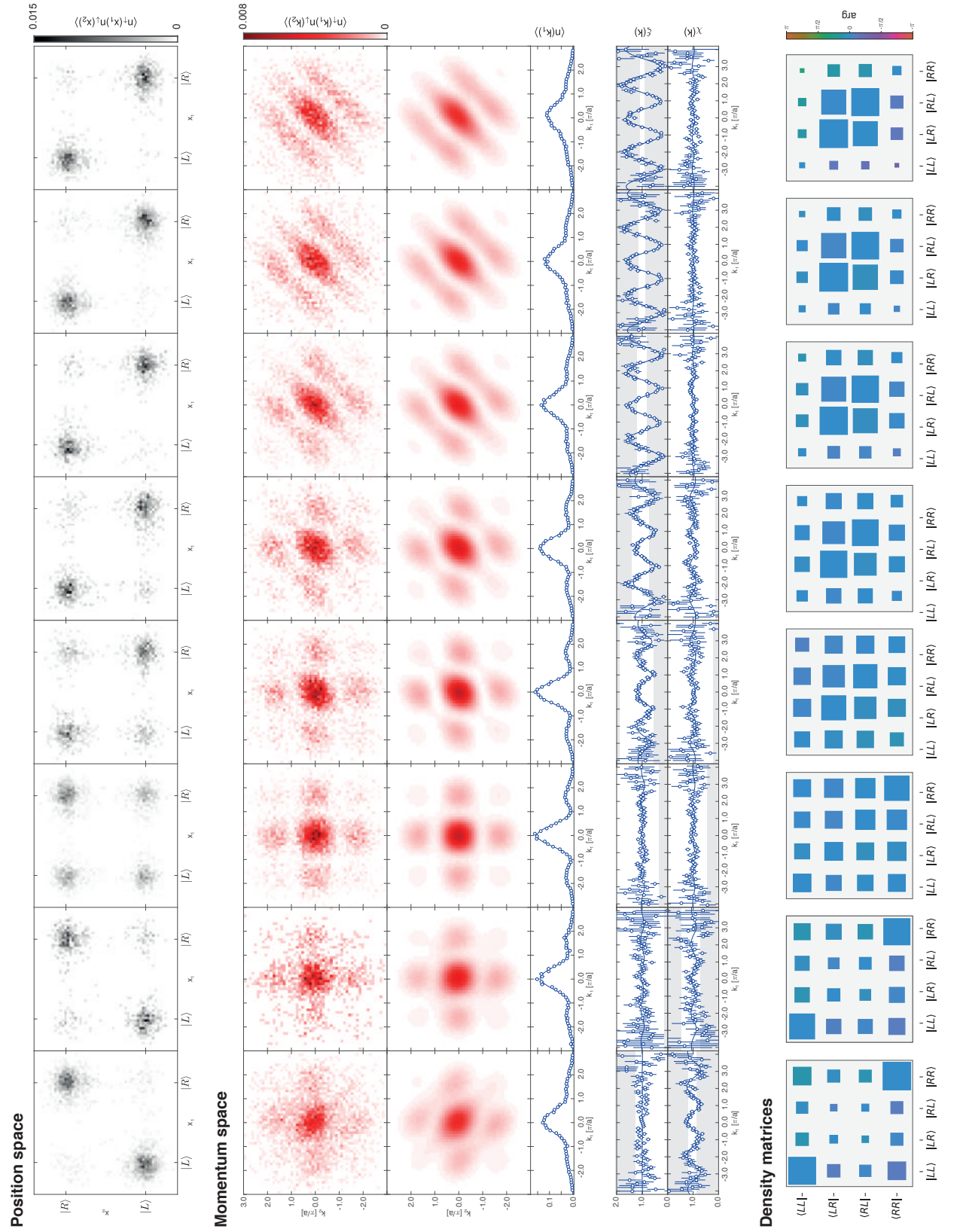


FIG 9. Full data set. Insitu (top) and momentum space correlations (middle) for all measured interaction strengths. From left to right, the magnetic offset field tunes the interactions from attractive (525 G) through zero (568 G) to the strongly repulsive regime (625 G). The bottom row shows the reconstructed density matrices $\hat{\rho}_{\text{BME}}$.